Available online at www.sciencedirect.com
ScienceDirect
Vacuum 81 (2006) 401–410
VACUUM
SURFACE ENGINEERING, SURFACE INSTRUMENTATION & VACUUM TECHNOLOGY
www.elsevier.com/locate/vacuum

Analysis of the flow in grooved pumps with specified pressure boundary conditions

Yeng-Yung Tsui*, Shiaugh-Ping Jung

Department of Mechanical Engineering, National Chiao Tung University, Hsinchu 300, Taiwan, ROC

Abstract

In this study the numerical method is employed to examine the flow in pumps with spiral grooves. A methodology suitable for the use of unstructured grids is developed. In order to have the greatest feasibility, the governing equations are formulated in such a manner that the grids are allowed to rotate with the rotor. Different from common practices, pressures are specified on the inlet and the outlet boundaries. Therefore, special treatments are required to calculate the mass flow rate and the inlet and outlet velocities. The methodology developed here is assessed via comparison with existing measurements and good agreement is obtained. Examination of pump parameters reveals that in order to obtain maximum flow rate, both the spiral angle and the groove height need to be carefully determined. The force balance over the entire flow channel shows that for a fixed pressure rise across the pump, the pressure difference between side walls is proportional to tangent of the spiral angle and the groove width, but inversely proportional to the groove height and the rotor length. These relationships can roughly be seen in the calculated results.

Keywords: Molecular pumps; Grooved pumps; Slip flows; Pressure boundary conditions; Unstructured grids

1. Introduction

Molecular pumps, such as the Gaede, Holweck, and Siegbahn types, feature flow grooves mounted on a rotational cylinder or disc. By replacing the reference frame on the rotor, the grooves become stationary with a moving upper wall. When molecules collide with the moving wall, the velocity of the wall is imposed on the molecules. Thus, the molecules have a higher probability to go in the direction from the inlet to the outlet. From a continuum point of view, momentum is transferred to the gas by diffusion in the near wall region. The shear stress is balanced by an adverse pressure gradient, resulting in increase of pressure along the channels.

In the Holweck and Siegbahn pumps the direction of the moving wall is inclined to the flow channels. As illustrated in Fig. 1, the moving velocity can be divided into two orthogonal components, one along the channel and the other in the transverse direction crossing the channel. As a consequence, pressure builds up not only along the channel, but also across the space between the two side walls. The pressure rise Δp_x between the inlet and the outlet is related to the pressure difference Δp_w between the side walls:

$$\Delta p_x WH = \Delta p_w L' H \cos\alpha - F_x, \tag{1}$$

where $L' = L/\sin\alpha$. The above equation, which ignores the clearance gap and the difference of the momentum fluxes between the inflow and the outflow, represents the force balance over the channel in the axial direction. The equation expresses that the pressure rise in the pump depends on the side-wall pressure difference Δp_w and the geometric parameters: pump length L, groove width W, groove height H and spiral angle α .

As seen from the above equation, the pressure rise is increased as the spiral angle decreases. However, it was shown [1,2] that when the angle decreases, the side-wall pressure difference is reduced due to the reduction of both the transverse component of the wall velocity and the transverse width between the side walls. As for the channel height, the increase of this height leads to increase of momentum transfer to the flow from the moving wall because the average velocity in the channel becomes lower

*Corresponding author.
E-mail address: yytsui@ail.nctu.edu.tw (Y.-Y. Tsui).

0042-207X/$ - see front matter © 2005 Published by Elsevier Ltd.
doi:10.1016/j.vacuum.2005.09.008

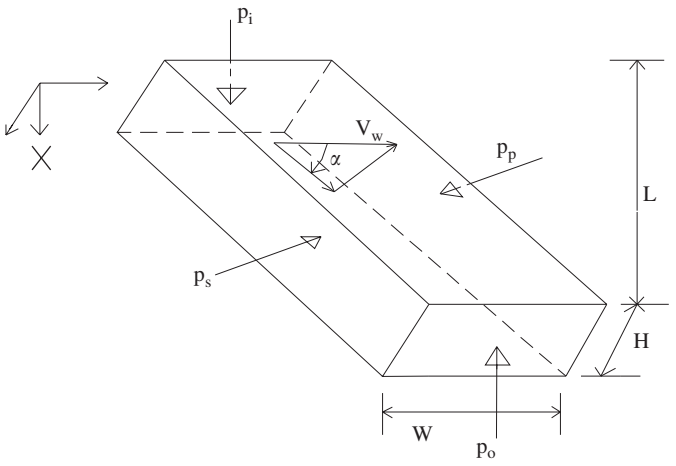

Fig. 1. Illustration of force balance over a flow channel. L: channel length in the x-direction, H: channel height, W: channel width, α: spiral angle, V_w: top wall speed, p_i: inlet pressure, p_o: outlet pressure, p_s: suction side pressure, p_p: pressure side pressure.

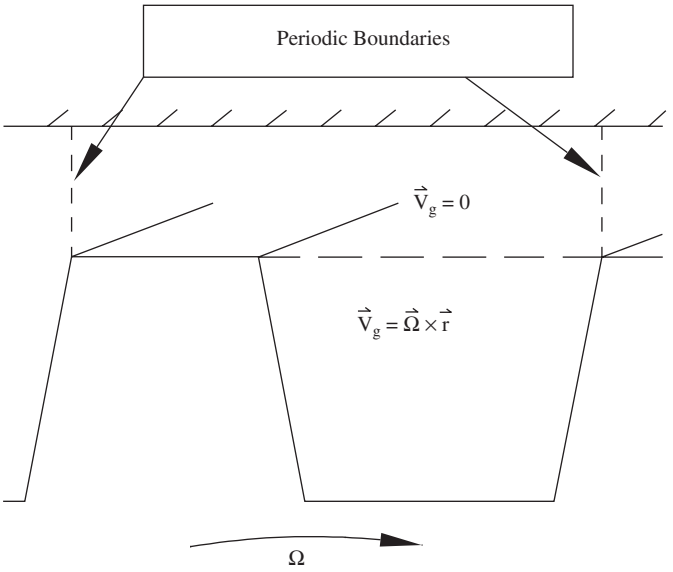

Fig. 2. Illustration of the flow channel for computations.

provided that the mass flow rate remains constant. A negative impact on the pumping performance is that reversed flow may appear [1,2]. The increase of the channel width also has pros and cons. With a large value of width the transverse pressure gradient will have more space to build up [1,2]. But, seen from the equation, the pressure rise is inversely proportional to the width. Based upon these considerations, it can be concluded that these parameters need to be optimized to achieve the best performance.

In the above discussion it is assumed that the mass flow rate through the pump is known beforehand, and it is the pressure rise between the inlet and the outlet being sought. Another kind of problem encountered is that with the pressure rise given, the mass flow rate needs to be determined. Unlike the former problem, there is no explicit expression to relate the mass flow rate with the side-wall pressure difference and the geometric parameters.

In this study a computational method is employed to investigate the flow in the spiral grooves of a vacuum pump under specified pressure conditions. Because the mass flux is not known a priori, special treatments are required to calculate the velocities from the pressure conditions at the inlet and outlet boundaries. Different from our previous studies [1–3], in which structured grids with curvilinear coordinates were adopted, a methodology suitable to unstructured meshes is developed.

2. Mathematical method

There are a number of grooves placed on the rotor of the pump. Since these grooves are arranged in the periodic manner, only one flow groove is considered in the calculation. A schematic sketch of the computational channel is shown in Fig. 2. The channel is divided into two parts: the groove region and the clearance region. The groove rotates with the rotor while the clearance between the housing and the rotor remains stationary. In order to cope with this situation the mass and momentum equations are cast into the Lagrangian–Eulerian form:

$$\nabla \bullet [\rho(\vec{V} - \vec{V}_g)] = 0, \tag{2}$$

$$\nabla \bullet [\rho(\vec{V} - \vec{V}_g) \times \vec{V}] = \nabla \bullet (\mu \nabla \times \vec{V}) + \vec{q}. \tag{3}$$

Here $\vec{V}_g$ is the grid velocity. The grid velocity is set to zero in the clearance region and the rotational velocity is assigned to $\vec{V}_g$ in the groove region (see Fig. 2). It is noted that the flows in both regions are assumed to be steady and there is no relative motion between the two regions despite the grid velocity imposed upon the groove region. Due to the periodic arrangement of the grooves, periodic conditions are prescribed on the two sides of the clearance region. Namely, mass and momentum into and out of the two periodic boundaries must be consistent. In addition, the pressures on these boundaries must be identical.

The pumping flow is assumed to be isothermal. Therefore, the energy equation is not required in calculations. However, there exists a large variation in density in the pumping process. The equation of state has to be considered:

$$p = \rho RT. \tag{4}$$

2.1. Discretization of the transport equations

After the domain is partitioned into a number of arbitrary polyhedrons, difference transport equations can be obtained by integrating the differential equation (3) overreach of the polyhedral cells:

$$\sum_f (\rho(\vec{V} - \vec{V}_g) \bullet \vec{s})_f \vec{V}_f = \sum_f (\mu(\nabla \otimes \vec{V}) \bullet \vec{s})_f + \vec{q}\Delta v, \tag{5}$$

where the subscripts f denote the values through the face f, $\vec{s}_f$ is the surface vector of the face, and the summations are over all the faces of the P-cell under consideration (see Fig. 3).

The approximation for the face value in the convection flux is crucial to computational accuracy. The scheme adopted here is the one mixing the upwind difference and a second-order difference:

$$\vec{V}_f = \vec{V}^{UD} + \gamma(\nabla \otimes \vec{V})^{UD} \bullet \vec{\delta}, \tag{6}$$

where the superscripts UD denote the node in the upwind direction of the face under consideration, $\vec{\delta}$ is the distance vector directed from the upwind node to the centroid of the face, and γ is a value ranging between 0 and 1.

There are a number of formulations for the diffusion flux [4–8]. It has been shown by Tsui [9] that the one employed in the following is virtually equivalent to these expressions, but it is much easier to implement, regardless of two-dimensional or three-dimensional problems. It was first proposed by Jasak [10] to separate the diffusion flux into the following two parts:

$$(\mu(\nabla \otimes \vec{V}) \bullet \vec{s})_f = \mu_f(\nabla \otimes \vec{V}_f) \bullet \vec{d} + \mu_f(\nabla \otimes \vec{V}_f) \bullet (\vec{s}_f - \vec{d}). \tag{7}$$

In this equation $\vec{d}$ is defined as

$$\vec{d} = \frac{s_f^2}{\vec{\delta}_{PC} \bullet \vec{s}_f} \vec{\delta}_{PC}, \tag{8}$$

where δ_{PC} is the vector connecting the point P and its neighboring point C (see Fig. 2). The diffusion flux is then approximated by

$$(\mu\nabla \otimes \vec{V} \bullet \vec{s})_f = \frac{\mu_f s_f^2}{\vec{\delta}_{PC} \bullet \vec{s}_f} (\vec{V}_C - \vec{V}_P) + \mu_f \overline{\nabla \otimes \vec{V}_f} \bullet (\vec{s}_f - \vec{d}). \tag{9}$$

The second term on the right-hand side is referred to as the cross-derivative of the diffusion, which arises in non-orthogonal grids. The overbar means that this gradient is obtained via interpolation from the velocity gradients on the two points P and C adjacent to the considered face.

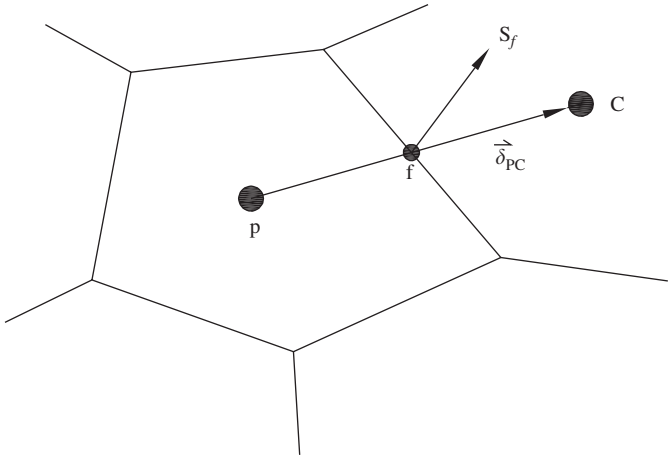

Fig. 3. A typical control volume and its surrounding cells.

Using the above treatments, the following discrete momentum equation is obtained:

$$\vec{V}_P = \vec{H}(V_C) - D_P \nabla p, \tag{10}$$

where

$$\vec{H}(V_C) = \frac{1}{A_P}\left[\sum_C A_C \vec{V}_C + \vec{Q}\right], \tag{11a}$$

$$D_P = \frac{\Delta v}{A_P}. \tag{11b}$$

The subscripts C designate the neighboring nodes of the node P under consideration and the summation is over all these nodes. The source term $\vec{Q}$ contains all sources other than the pressure gradient, including the cross-diffusion term seen in Eq. (9). The pressure gradient is approximated as

$$\nabla p = \frac{1}{\Delta v} \sum_f p_f \vec{s}_f, \tag{12}$$

where p_f is the pressure on the face f and is obtained by linear interpolation from the two nodes at the two sides of the face.

2.2. Calculation of face velocity and mass flow rate

In the mesh system the velocity and the pressure are stored at cell centers. The velocity, or the mass flow rate, on each face is required for mass conservation in the cell and for calculation of the convection flux shown in Eq. (5). It is well known that a simple interpolation of velocity from the two nearby nodes will lead to solutions with inherent checkboard oscillations. To circumvent this, a method similar to that of Rhie and Chow [11] is used:

$$\vec{V}_f = \overline{\vec{V}_f} - (D_f \nabla p_f - D_f \overline{\nabla p_f}), \tag{13}$$

where the face values with overbars on the right-hand side are obtained via interpolation from the two adjacent nodal values and D_f is obtained by averaging over the two cells. The mass flow rate across the face is then approximated by

$$\dot{m}_f = \overline{\rho}_f(\overline{\vec{V}}_f - \vec{V}_g) \bullet \vec{s}_f - A_C^P[(p_C - p_P) - \overline{\nabla p}_f \bullet \vec{\delta}_{PC}], \tag{14}$$

where A_C^p is defined by

$$A_C^p = \overline{\rho}_f D_f \frac{s_f^2}{\vec{\delta}_{PC} \bullet \vec{s}_f}. \tag{15}$$

2.3. Pressure-correction equation

The velocity, denoted as $\vec{V}^*$, obtained from solving the momentum transport equation (10), does not, in general, obey the mass conservation law. In the SIMPLE algorithm,

a pressure-correction equation can be derived by forcing a corrected velocity $\vec{V}^{**}$ to satisfy the continuity constraint. Following Patankar [12], the velocity correction is assumed to be linearly related to the pressure correction:

$$\vec{V}_f^{**} - \vec{V}_f^{*} = -D_f \nabla p_f'. \tag{16}$$

The correction of the mass flux is then give by

$$\begin{aligned} \dot{m}_f^{**} - \dot{m}_f^{*} &= -\overline{\rho}_f D_f \nabla p_f' \bullet \vec{s}_f \\ &= -\overline{\rho}_f D_f \nabla p_f' \bullet \vec{d} - \overline{\rho}_f D_f \overline{\nabla p_f'} \bullet (\vec{s}_f - \vec{d}) \\ &= A_C^p (p_P' - p_C') - \overline{\rho}_f D_f \overline{\nabla p_f'} \bullet (\vec{s}_f - \vec{d}). \end{aligned} \tag{17}$$

Let $\dot{m}^{**}$ on all faces surrounding the cell under consideration satisfy the continuity requirement. A pressure-correction equation is obtained:

$$A_P p_P' = \sum_C A_C p_C' + S_{p1} + S_{p2}, \tag{18}$$

where

$$S_{p1} = -\sum_f m_f^{*}, \tag{19a}$$

$$S_{p2} = \sum_f \overline{\rho}_f D_f \overline{\nabla p_f'} \bullet (\vec{s}_f - \vec{d}). \tag{19b}$$

In Eq. (18) the superscripts p appearing in the coefficients are omitted. It is noted that the S_{p1} represents the mass imbalance in the cell and the second term, arising from the irregular mesh, represents the cross-derivative as seen in the diffusion flux given in Eq. (9). During iteration to obtain solution, the S_{p2} term can be ignored provided that the iterative procedure converges. However, as the mesh becomes extremely ''skew'', inclusion of the cross-derivative term could help to stabilize the iterative procedure or accelerate the convergence rate. To account for the S_{p2} term, a successive correction procedure can be employed [9].

2.4. Pressure considerations at the boundary

In this study, static pressures are imposed on the inlet and outflow boundaries. The mass flux through the inlet can be calculated in a manner similar to Eq. (14) for the face flux (see Fig. 4).

$$\begin{aligned} \dot{m}_{in} = \overline{\rho}_b (\vec{V}_{in} - \vec{V}_g) \bullet \vec{s}_b - \rho_b D_P \\ \times \frac{s_b^2}{\vec{\delta}_{Pb} \bullet \vec{s}_b} [(p_b - p_P) - \nabla p_b \bullet \vec{\delta}_{Pb}]. \end{aligned} \tag{20}$$

The intake velocity $\vec{V}_{in}$ and the pressure gradient at the boundary ∇p_b can be estimated through extrapolation from interior nodes. To estimate $\vec{V}_{in}$, zero gradients are assumed. As for calculation of ∇p_b, a linear extrapolation approach is used. It is noted that this linear extrapolation uses two interior points adjacent to the boundary in the structured grid system. However, with unstructured grids, the extrapolation is not nearly as straightforward because the next nearest neighbor point is not easy to identify.

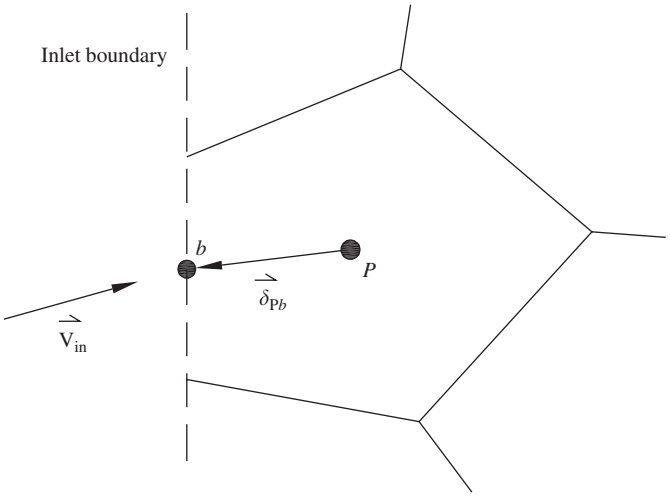

Fig. 4. An inlet boundary cell.

Instead, the following relation is used to calculate the boundary value:

$$\phi_b = \phi_P + \nabla \phi_P \bullet \vec{\delta}_{Pb}, \tag{21}$$

where ϕ stands for the pressure gradient ∇p. The gradient of ϕ at point P can be expressed as

$$\nabla \phi_p = \frac{1}{\Delta v} \sum_f \phi_f \vec{s}_f = \frac{1}{\Delta v} \left[\phi_b \vec{s}_b + \sum_{f \neq b} \phi_f \vec{s}_f \right]. \tag{22}$$

Here, the summation in the brackets is taken over all the surrounding faces except for the boundary one. Substituting this expression into Eq. (21) leads to

$$\phi_b = \frac{\phi_P + (1/\Delta v) \sum_{f \neq b} \phi_f \vec{s}_f \bullet \vec{\delta}_{Pb}}{1 - (1/\Delta v) \vec{s}_b \bullet \vec{\delta}_{Pb}}. \tag{23}$$

It is noted that the above method is also used to calculate pressure on all the boundaries.

After the pressure-correction Eq. (18) is solved for the pressure correction p', the intake mass flux is adjusted in the following way:

$$\dot{m}_{in}^{**} = \dot{m}_{in}^{*} - \rho_b D_P \frac{s_b^2}{\vec{\delta}_{Pb} \bullet \vec{s}_b} (p_b' - p_P'), \tag{24}$$

where p_b' is obtained using the same extrapolation procedure given in Eq. (23).

Although the velocity at the outflow boundary can be treated in the same manner described above, it is not necessary to do so because the overall mass flow rate has been determined at the inlet. Therefore, a simple extrapolation method, say, zero velocity gradient, can be done. In order to ensure overall mass conservation as well as to accelerate convergence, a global adjustment of the outgoing velocity is carried out after each iteration such that the total mass flow rates at both inlet and outlet are identical.

It must be pointed out that the pressure on the plane of either the inlet or the outlet boundary is not uniformly

distributed in the present calculation. The pressure values at the computational nodes on the boundary planes are first obtained using the extrapolation given by Eq. (23). These pressures are then adjusted in such a way that the overall average pressure on the plane is equal to the imposed pressure. In this way the pressures on the boundaries are floating, which is beneficial to convergence and is physically more correct. Another point that needs to be clarified is that a reference node is selected on the outflow boundary plane. After solving the pressure-correction equation, the p' at this node is set to zero and the pressure corrections for all other nodes are changed accordingly. Hence, the pressure level is close to the specified pressure without much change after each iteration.

3. Results and discussion

To validate the above method, the flow in a benchmark pump is calculated. Computed results are compared to the available experimental data and the flow structure is illustrated. The method is then applied to a pump to investigate the effects of pump parameters.

3.1. Validation of the method

A schematic sketch of a typical pump is shown in Fig. 5. The validation case is a pump with six grooves. The rotor rotates at 18 000 rpm. The geometric parameters are given as: axial length of the pump $L = 115$ mm, outer diameter of the rotor $D = 137$ mm, groove height $H = 4.06$ mm, groove width $W = 52.5$ mm, clearance gap $C = 0.65$ mm, and spiral angle $\alpha = 15°$. Measurements required for validation of the predictions were reported in Ref. [13].

In the following tests the pressure level in the pump is within the limits of 0.1 and 1 torr (13.3 and 133 Pa). At this level the Knudsen number (defined as the ratio of the mean free path of the gas to the height of the channel) roughly lies in the range between 0.1 and 1, which corresponds to the slip flow regime. Hence, a slip velocity V_0 imposed on all the solid walls in the calculation, given as

$$V_0 = V_w + \lambda\left(\frac{\mathrm{d}V}{\mathrm{d}y}\right)_w, \tag{25}$$

where V_w is the velocity of the solid wall itself, $(\mathrm{d}V/\mathrm{d}y)_w$ the velocity gradient of the flow at the wall, and λ the mean free path of the gas.

In the first series of tests the pressure at outlet is specified at 1 torr (133 Pa), whereas that at the inlet is fixed at a number of values less than the outlet pressure (0.5, 0.7, and 0.9 torr). The resulting mass flow rates, in terms of sccm, are presented in Fig. 6. Comparison with experiments indicates that both agree well with each other. Additional data to validate the computational method can be found in Fig. 7. In this second series of tests the same pressures (0.1, 0.3, and 1 torr) are specified at the inlet and the outlet boundaries. This corresponds to the maximum flow rate condition.

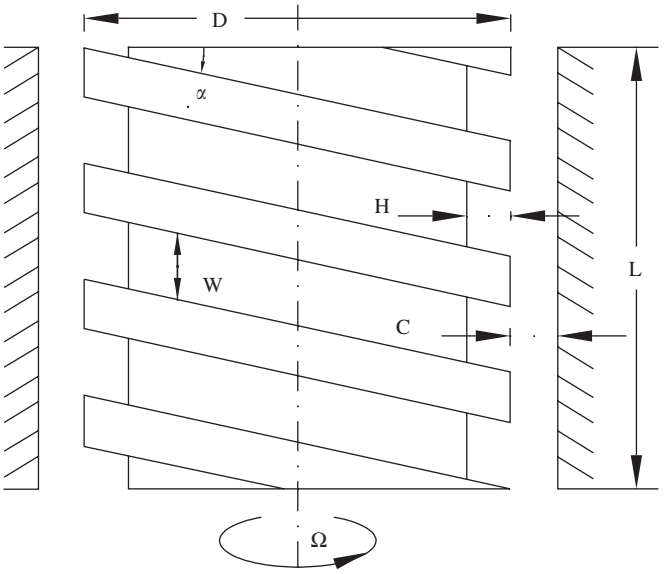

Fig. 5. A schematic drawing of the pump. D: rotor diameter, L: rotor length, C: clearance, α: spiral angle, W: groove width, H: groove height, Ω: rational speed.

The calculated velocities at inlet and outlet planes using the moving grid method described in the last section are presented in Figs. 8a and 9 for the case with 0.5 torr at inlet and 1 torr at outlet. The secondary flow illustrated in Fig. 8a behaves like a Couette flow driven by the rotating rotor. It is more common to place the frame of reference on the rotor and, thus, the flow is driven by the housing wall rotating in the opposite direction. With this moving top wall and using an analogous procedure to that presented above, but with $\vec{V}_g = 0$, the resulting flow is shown in Fig. 8b. Results from these two calculations agree well in view of the difference of the reference frames. The axial velocity is illustrated in contour plots shown in Fig. 9. In comparing to the inlet flow, the velocity at the outlet face becomes more uniformly distributed. It is observed that reversed flow prevails in the clearance gap throughout the channel, which can be ascribed to the adverse pressure gradient imposed on the pump. The pressure distribution at the two open boundaries is shown in Fig. 10. As stated in the last section, the pressure over these boundaries is not fixed; spatial variation is allowed in the present method. As seen from the figure, with a peak pressure located near the left wall of the groove, the pressure gradually decreases in both the groove and the clearance. The wall with high pressure on the left of the groove is termed the pressure side, whereas the wall with low pressure on the right the suction side. Although the pressure distribution is non-uniform, the average pressures over the planes are fixed at the given values of 0.5 and 1 torr, respectively, for the inlet and the outlet boundaries.

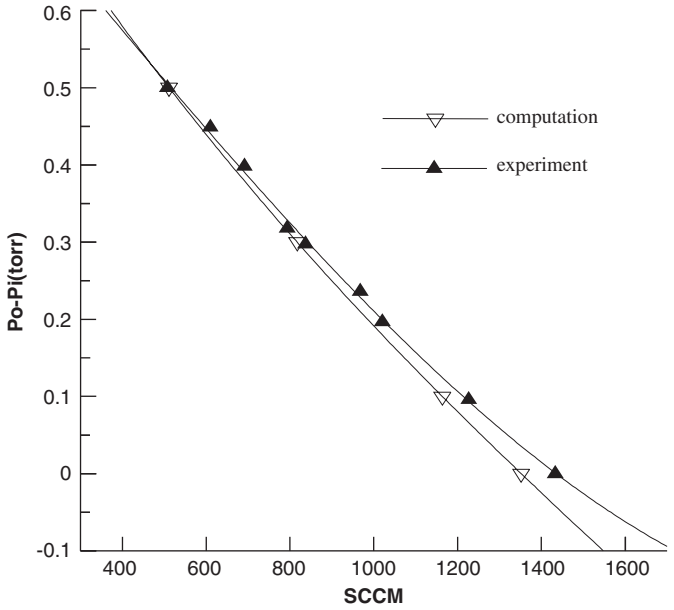

Fig. 6. Comparison of flow rate with experiments for the cases with outlet pressure $p_o = 1$ torr and inlet pressures $p_i = 0.5, 0.7, 0.9$, and 1 torr.

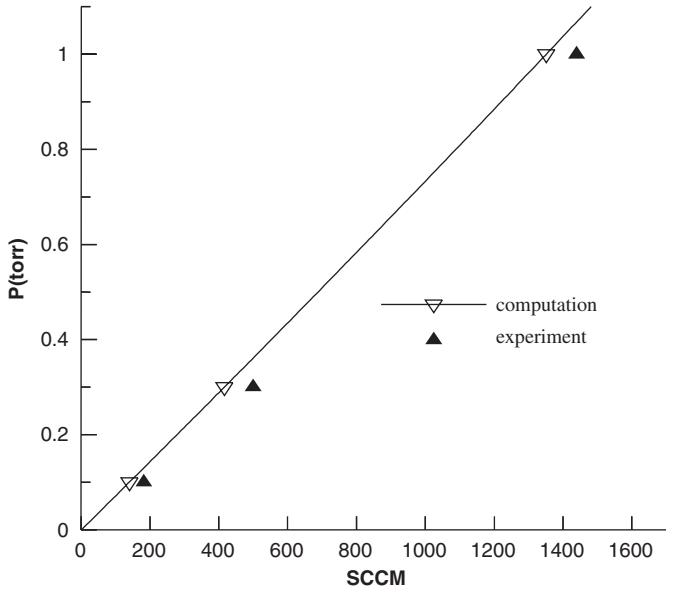

Fig. 7. Comparison of flow rate with experiments for the cases with $p_i = p_o = 0.1, 0.3$, and 1 torr.

3.2. Parametric tests

In these tests the following parameters are used as a test case: axial length $L = 40$ mm, outer diameter of the rotor $D = 50$ mm, groove height $H = 1$ mm, groove width $W = 16.2$ mm, clearance gap $C = 0.2$ mm, spiral angle $\alpha = 14.28°$, and angular speed $\Omega = 18\,000$ rpm. The pressures of 9835 and 10 130 Pa are specified at the inlet and the outlet boundaries, respectively. According to Sawada et al. [14], the flow at this pressure level is in the laminar regime. In the following, the pump configuration is modified to examine its effects on the flow rate. The parameters considered in the modification are the groove height, groove width, clearance gap, spiral angle, and angular speed.

(a) *Tests of spiral angle*: The calculated flow rates corresponding to four spiral angles are shown in Table 1. The flow rate increases as the spiral angle decreases from 18.28° to 10.28°, followed by a decrease for the angle being further reduced to 8.28°. The change of the spiral angle has two contrasting effects on the flow. As illustrated in Fig. 1, by situating the reference frame on the rotating shaft, the flow channel can be regarded as stationary, but with a moving top wall. When the spiral angle decreases, the wall velocity component, in the direction along the channel, increases. This results in greater inlet velocity and, thus, larger flow rate. The decrease of the angle also leads to a decrease in the opposing pressure gradient because the pressure rise through the channel is fixed and the channel length becomes longer. It can be seen from Fig. 11 that owing to the larger flow velocity and smaller opposing pressure gradient, the reversed flow in the groove is much weaker for $\alpha = 8.28°$ when compared with $\alpha = 18.28°$. However, it should be noticed that the normal width of the channel groove decreases with the spiral angle. This has the effect of hampering the gas flow. It needs to be mentioned here that for the sake of better illustration, the height of the channel in Fig. 11 and the following figures is magnified by a factor of 2.5.

(b) *Tests of groove height*: It is expected that the flow rate increases with the groove height due to the enlarged cross-sectional area, which is demonstrated in Table 2 when the height is changed from 0.4 to 0.6 mm. But, the flow becomes prone to separation since the momentum transport from the moving wall by the shear stress becomes less effective. As seen in Fig. 12 for the height of 1.4 mm, a strong flow separation takes place in the main part of the channel and, thus, the flow rate becomes negative in Table 2.

(c) *Tests of groove width*: The width of the groove is inversely proportional to the number of grooves. The number of grooves used for tests are 4, 5, and 6. In spite of the differences in the groove numbers, the total area of the grooves remains the same. The flow rates shown in Table 3 are for the entire pump, not for a single flow channel. According to this table, the flow rate increases as the number of grooves is reduced because of enlarged space in the grooves.

(d) *Tests of clearance gap*: It has been seen in the above figures that reversed flow always prevails in the clearance region. It is clear in Fig. 13 that without the clearance gap, there is no flow separation at all and, as given in Table 4, the flow rate is extremely high. When the gap is increased, the reversed flow is strengthened and the flow rate is greatly reduced. The worst happens at the gap of 0.3 mm, for which the reversed flow covers a large part of the channel (Fig. 13) and the flow rate becomes negative (Table 4).

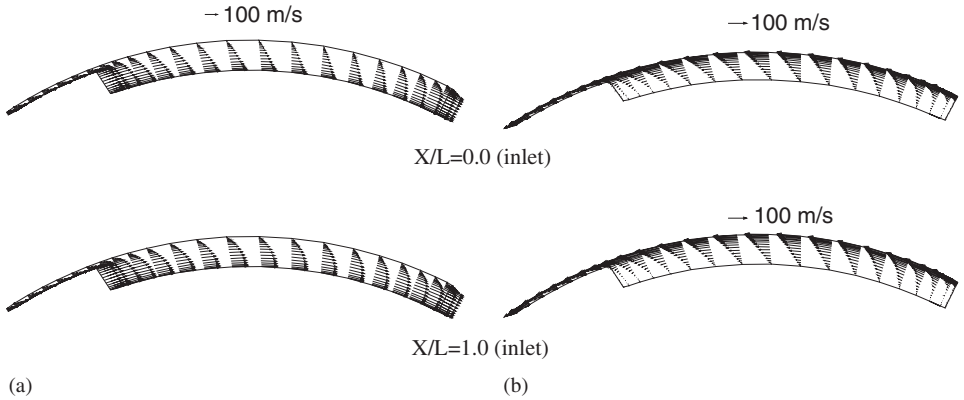

Fig. 8. Secondary velocity vectors on the inlet ($x/L = 0$) and outlet ($x/L = 1$) planes: (a) moving-grid calculation; (b) moving-wall calculation.

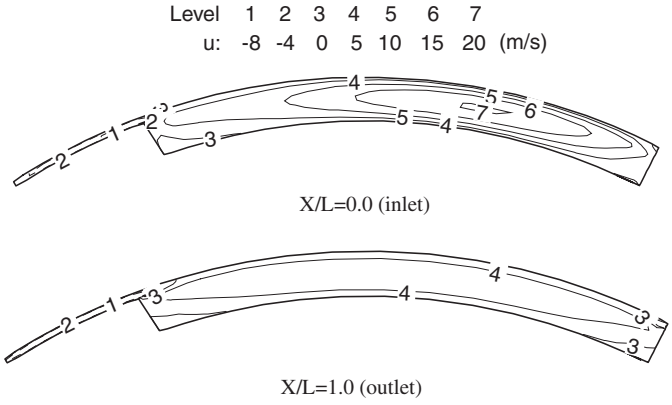

Fig. 9. Axial velocity contours on the inlet ($x/L = 0$) and outlet ($x/L = 1$) planes.

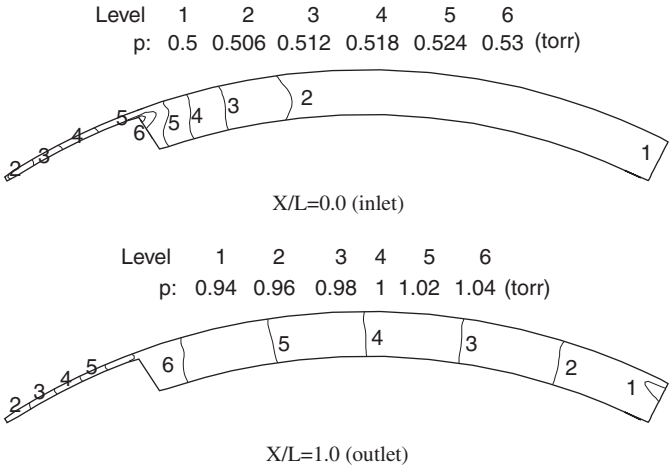

Fig. 10. Pressure distribution on the inlet ($x/L = 0$) and outlet ($x/L = 1$) planes.

Table 1
Flow rates and side-wall pressure differences for various spiral angles

Spiral angle α	8.28°	10.28°	14.28°	18.28°
Flow rate (sccm)	281.7	373.5	343.5	48
Δp_w (Pa)	18.8	23.3	32.6	41.8

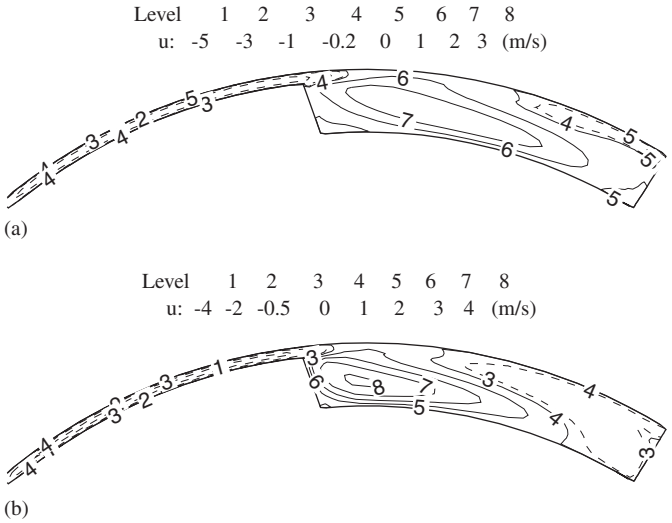

Fig. 11. Axial velocity contours at $x/L = 0.4$ for different spiral angles: (a) $\alpha = 8.28°$, (b) $\alpha = 18.28°$.

Table 2
Flow rates and side-wall pressure differences for various groove heights

Groove height H (mm)	0.4	0.6	1.0	1.4
Flow rate (sccm)	193.4	407.9	343.5	−362.6
Δp_w (Pa)	37.4	34.9	32.6	31.3

(e) *Tests of rotational speed*: As shown in Table 5, the flow rate increases with the rotational speed of the pump. This is just what we expect because more momentum is transferred to the gas when the speed increases. At the two low speeds the flow rate is negative since reversed flow dominates in the channel, which is evident in Fig. 14. The

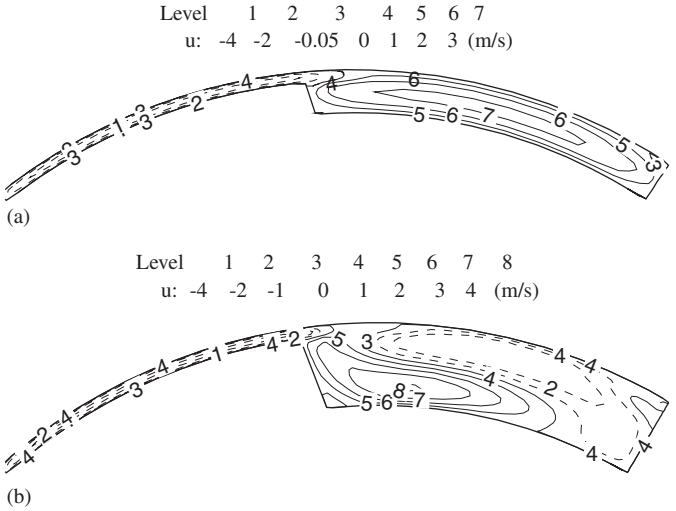

Fig. 12. Axial velocity contours at $x/L = 0.4$ for different groove heights: (a) $H = 0.6$ mm, (b) $H = 1.44$ mm.

Table 3
Flow rates and side-wall pressure differences for various groove numbers

No. of grooves	4	5	6
Flow rate (sccm)	389.4	343.5	295.6
Δp_w (Pa)	40.7	32.6	27.1

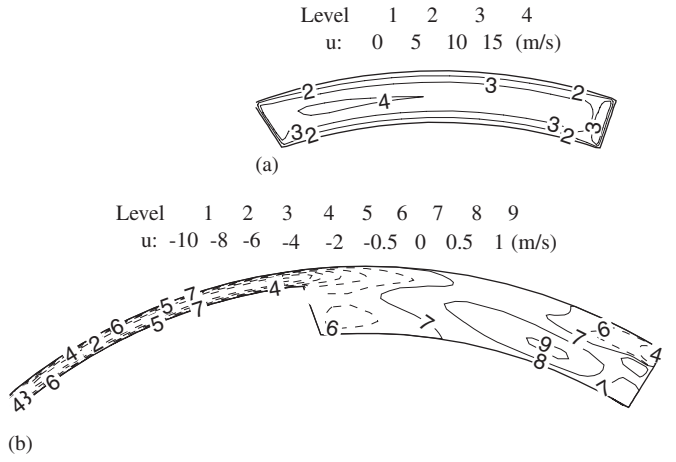

Fig. 13. Axial velocity contours at $x/L = 0.4$ for different clearances: (a) $C = 0$ mm, (b) $C = 0.3$ mm.

cause of the reversed flow is ascribed to the fact that the momentum transferred form the moving wall is too low to overcome the attendant adverse pressure gradient.

3.3. Effects of geometrical parameters on the side-wall pressure difference

The force balance equation (1) can be rewritten as

$$\Delta p_w = \frac{\tan\alpha}{L}\left(W\Delta p_x - \frac{F_x}{H}\right). \tag{26}$$

Table 4
Flow rates and side-wall pressure differences for various clearance gaps

Clearance gap C (mm)	0.0	0.1	0.2	0.3
Flow rate (sccm)	4685.0	1311.5	343.5	−908.1
Δp_w (Pa)	42	33.6	32.6	31.8

Table 5
Flow rates for various rotational speeds

Rotational speed Ω (rpm)	6000	12 000	18 000	24 000
Flow rate (sccm)	−1190.7	−495.0	343.5	1244.5

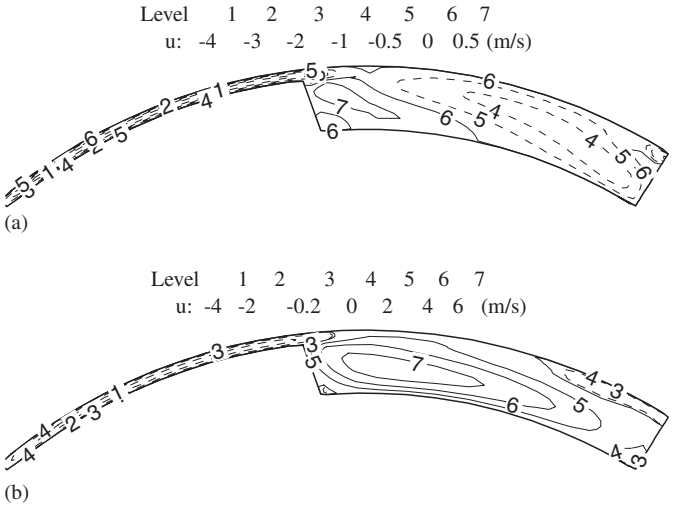

Fig. 14. Axial velocity contours at $x/L = 0.4$ for different rotational speeds: (a) 12 000 rpm, (b) 24 000 rpm.

By assuming a constant pressure rise and a constant frictional force, the following correlations can be seen:

$$\Delta p_w \propto \left(\tan\alpha, W, \frac{1}{H}, \frac{1}{L}\right). \tag{27}$$

Although the frictional force does depend upon the geometrical parameters, the correlations above can serve as an indication of how the side-wall pressure difference changes with these parameters. Such correlations are particularly valid under non-viscous flow conditions where the viscosity can be ignored. Then Δp_w is independent of the groove height, H.

With the increase of the spiral angle, both the width normal to the channel and the normal velocity component of the moving wall are increased. This helps the transverse pressure gradient to develop, which is evident in Table 1.

The pressure forces exerted on both the inlet and the outlet boundaries and on the side walls are directly proportional to the groove height. However, the dependence of the frictional force on the groove height is much

weaker. In order to have a balance between these forces, as given in Eq. (1), the side-wall pressure difference is inversely proportional to the groove height, as shown in Table 2.

When the width of the groove is increased, there is more room for the pressure gradient to develop. As a consequence, Δp_w increases with the width, which can be seen in Table 3.

For fixed inlet and outlet pressures, the pressure gradient along the channel becomes smaller as the channel length increases. To balance this pressure gradient the transverse pressure gradient is also decreased. Hence, Δp_w is inversely proportionally to the length.

The effect of clearance cannot be shown in the force balance equation. However, it can be imagined that with the clearance gap, there will be gas leaking from the pressure side to the suction side through the gap, which will result in reduction of the pressure difference between the two sides. This is clearly shown in Table 4.

4. Conclusions

A methodology has been developed to deal with the flow in grooved pumps with fixed boundary pressures. The formulation is based on a moving grid concept and unstructured meshes are incorporated in the method. An approximation to the momentum equation is employed for calculating the intake velocity, or the intake flow rate, while the outgoing velocity is obtained via an extrapolation procedure. In the present method the pressure is not uniformly distributed over the open boundaries. It is the overall average pressure fixed at the specified value. With this method, good agreement, in terms of mass flow rate, is obtained, when compared with measurements. However, the experimental data available are limited to the situation with positive mass flow rate through the pump. It was shown in our calculations that reversed flow prevails in the clearance gap. In some cases with large groove heights or clearances, or with low rotational speeds, the reversed flow overwhelms the flow field, resulting in negative flow rate. Therefore, extensive experimental work is definitely needed to provide further justification for the present numerical procedure. Tests on pump parameters show the following findings:

(1) In general, the reduction of the spiral angle brings about higher flow rate because of the increased velocity component in the channel direction and the decreased adverse pressure gradient. But, on the other hand, the reduced transverse space will hinder the flow.
(2) The increase of groove height leads to larger cross-sectional area and, thus, greater flow rate. However, the negative impact is that the flow tends to separate and the flow is limited.
(3) The flow rate is increased with the groove width when the number of grooves is reduced.
(4) It was confirmed in the calculations that the pressure difference between the side walls is increased with the spiral angle and the groove width, and decreased with the groove height and the clearance gap.

Acknowledgements

This work was partly supported by the National Science Council, ROC, under contract NSC 91-2212-E009-051. The financial support provided by the Precision Instrument Development Center of the National Science Council, ROC, for one of the authors is greatly acknowledged.

Appendix

Notation

A_P	main coefficient in discretized equations
A_C	coefficient connecting node C in discretized equations
$\vec{d}$	a vector in the direction of $\vec{\delta}_{PC}$
C	clearance gap
D	rotor diameter or pressure coefficient in discretized equations
F_x	frictional force in the axial direction
H	groove height
L	rotor length
L'	channel length
$\dot{m}$	mass flow rate
p, p'	pressure and pressure correction
p_i, p_o	pressures at the inlet and the outlet
p_p, p_s	pressures at the pressure side and the suction side
$\vec{q}$	source term of the momentum equation
$\vec{Q}$	source term of the discretized momentum equation
$s_f, \vec{s}_f$	surface area and surface vector
S_{p1}, S_{p2}	two source terms in the pressure-correction equation (18)
$\vec{V}$	velocity vector
$\vec{V}_g$	grid velocity
V_0	flow velocity on the wall
V_w	wall velocity
W	groove width
α	spiral angle
$\vec{\delta}$	a distance vector directed from a nodal point upstream of a face to the centroid of the face
$\vec{\delta}_{PC}$	a distance vector directed from a point P to a neighbor point C
$\vec{\delta}_{Pb}$	a distance vector directed from a point P to a boundary point b
Δv	volume of the cell under consideration
Δp_w	pressure difference between side walls $(p_p - p_s)$
Δp_x	pressure difference between inlet and outlet $(p_o - p_i)$
γ	a weighting value
λ	mean free path

μ viscosity
ρ density
Ω rotational speed of the pump

Subscripts

b a point on the boundary
C a point next to the main point P
f the interface between cells P and C
in inlet value
P main point

References

[1] Tsui Y-Y, Su Y-S, Cheng H-P. ASME J Fluids Eng 2002;124:287–90.
[2] Tsui Y-Y, Kung C-P, Cheng H-P. Numer Heat Transfer 2001;A40:73–88.
[3] Tsui Y-Y, Kung C-P. J Vac Sci Technol 2001;A19:2785–90.
[4] Lai YG. Numer Heat Transfer 1997;B32:267–81.
[5] Kim D, Choi H. J Comput Phys 2000;162:411–28.
[6] Hwang YH. Numer Heat Transfer 1995;B27:323–36.
[7] Rida S, McKenty F, Meng FL, Reggio M. Int J Numer Meth Fluids 1997;25:697–717.
[8] Davidson L. Int J Numer Meth Fluids 1996;22:265–81.
[9] Tsui Y-Y. In: Proceedings of the 10th National Conference CFD, Hua-Lien, Taiwan; 2003.
[10] Jasak H. PhD thesis, Imperial College, University of London; 1996.
[11] Rhie SCM, Chow WL. AIAA J 1983;21:1525–32.
[12] Patankar V. Numerical heat transfer and fluid flow. New York: McGraw-Hill; 1980.
[13] Nanbu K, Igarashi S. Comput Fluids 1992;21:221–8.
[14] Sawada T, Nakamura M, Abumiya A. Vacuum 1992;43:1097–9.